Heliyon 9 (2023) e13171

Contents lists available at ScienceDirect

Heliyon

journal homepage: www.cell.com/heliyon

Research article

Deep-learning based breast cancer detection for cross-staining histopathology images

Pei-Wen Huang [a,b], Hsu Ouyang [c], Bang-Yi Hsu [c], Yu-Ruei Chang [c], Yu-Chieh Lin [d,e], Yung-An Chen [d], Yu-Han Hsieh [e], Chien-Chung Fu [d], Chien-Feng Li [f,g], Ching-Hung Lin [h], Yen-Yin Lin [e], Margaret Dah-Tsyr Chang [a,e], Tun-Wen Pai [c,*]

[a] Institute of Molecular and Cellular Biology, National Tsing Hua University, Hsinchu, Taiwan
[b] Department of Pathology, Hsinchu Mackay Memorial Hospital, Hsinchu, Taiwan
[c] Department of Computer Science and Information Engineering, National Taipei University of Technology, Taipei, Taiwan
[d] Department of Power Mechanical Engineering, National Tsing Hua University, Taiwan
[e] JelloX Biotech Inc., Hsinchu, Taiwan
[f] Department of Medical Research, Chi Mei Medical Center, Tainan, Taiwan
[g] National Institute of Cancer Research, National Health Research Institutes, Tainan, Taiwan
[h] National Taiwan University Hospital Hsinchu Branch, Hsinchu, Taiwan

ARTICLE INFO

Keywords:
Breast cancer
Cross-staining
Artificial intelligence
Adaptive color segmentation
Color deconvolution
Computational pathology

ABSTRACT

Hematoxylin and eosin (H&E) staining is the gold standard for tissue characterization in routine pathological diagnoses. However, these visible light dyes do not exclusively label the nuclei and cytoplasm, making clear-cut segmentation of staining signals challenging. Currently, fluorescent staining technology is much more common in clinical research for analyzing tissue morphology and protein distribution owing to its advantages of channel independence, multiplex labeling, and the possibility of enabling 3D tissue labeling. Although both H&E and fluorescent dyes can stain the nucleus and cytoplasm for representative tissue morphology, color variation between these two staining technologies makes cross-analysis difficult, especially with computer-assisted artificial intelligence (AI) algorithms. In this study, we applied color normalization and nucleus extraction methods to overcome the variation between staining technologies. We also developed an available workflow for using an H&E-stained segmentation AI model in the analysis of fluorescent nucleic acid staining images in breast cancer tumor recognition, resulting in 89.6% and 80.5% accuracy in recognizing specific tumor features in H&E– and fluorescent-stained pathological images, respectively. The results show that the cross-staining inference maintained the same precision level as the proposed workflow, providing an opportunity for an expansion of the application of current pathology AI models.

1. Introduction

Surgical pathology diagnosis has been based on microscopic slides stained with hematoxylin and eosin (H&E) for a long time. Hematoxylin is used as a nuclear stain, and eosin is used as a counterstain for cytoplasmic components and the extracellular matrix. In general, H&E staining can clearly demonstrate the cell morphology, features, and cellular interactions and is used to cope with the

* Corresponding author.
E-mail address: twp@ntut.edu.tw (T.-W. Pai).

https://doi.org/10.1016/j.heliyon.2023.e13171
Received 19 October 2022; Received in revised form 13 January 2023; Accepted 19 January 2023
Available online 21 January 2023

most routine pathological examinations, including tumor diagnosis and staging [1,2]. H&E-stained microscopic slides can be stored permanently and be easily evaluated by different pathologists at different time points.

Although H&E-stained microscopic slides are convenient for the majority of clinical and laboratory uses, they do not sufficiently address all the requests and demands for increasing pathological classification and stratification. Other techniques, including special staining, immunohistochemistry (IHC), immunofluorescence (IF), flow cytometry, and molecular pathology, have been applied. IHC and IF are based on the immunologic antigen-antibody principle and techniques to label specific cellular components, including proteins, glycans, and small molecules. These techniques are helpful in detecting biomarker expression to identify gene mutations, tumor origins, and classification, and they provide further information for disease prognosis and treatment decision-making, including the use of chemotherapy, target therapy, or immunotherapy. In IHC, the target antigen is detected by observing the colored products produced by antibody-conjugated enzyme labels such as horseradish peroxidase or alkaline phosphatase interacting with chromogenic substances such as diaminobenzidine (DAB) and hematoxylin as a nuclear counterstain. IHC shows good correlation with H&E staining slides, and both can be examined using light microscopy, allowing IHC to be widely applied in clinical protein and morphological diagnosis, even in companion diagnostics of target therapy [3–5]. Regarding IF, different cellular components and biomarkers are labeled by differential antibodies tagged with fluorophores, and counterstaining by fluorescent dyes such as SYTO16 and DiD, with different emission spectra, and each signal is separately detected by a fluorescent microscope. Fluorescent morphologic features do not match with H&E-stained sections or IHC, and fluorescent signals fade away over time. Therefore, IF is not commonly used in daily practice. However, distinct fluorescent images of different cellular components reveal more specific and accurate multiplex staining; hence, they are applied to paraffin tissue sections, cultured cell lines, *in vivo* tissue monitoring, and 3D tissue imaging using dark-field microscopy. These features benefit biomedical discovery with the correlation of multiple biomarkers, even in a live sample or 3D structure, and such technology is advancing in clinical and biological research fields [6–8].

Traditionally, pathology diagnostics relies on the inspection of tissues on glass slides under a light microscope. In the 1990s, commercialized whole-slide imaging (WSI) scanners transformed the whole tissue slide into a digitalized image, and digital pathology is being used in many applications [9–11]. In addition to the benefits of easy management, lower storage requirements, and remote diagnostic capability, digital pathology also provides the opportunity to use image analysis techniques for diagnostic auxiliaries, leading to a new field called computational pathology (CPATH). Along with the rapid development of deep learning (DL) artificial intelligence (AI) technologies, CPATH algorithms are now capable of assisting pathologists in tasks ranging from basic quantification to complicated disease staging [12–15].

DL is an extremely data-demanding technology, and the performance of a DL-based algorithm usually requires qualified ground truth data for model construction. Thousands of images could be required, especially for weakly supervised or unsupervised learning DL-model development [16,17]. Such data requirements are not difficult for H&E model development because a digitalized pathology lab usually generates abundant H&E images in routine diagnostic processes. Recently, the Human Protein Atlas has also offered public access to tens of thousands of histopathological images of different tumor types [18]. However, in clinical research, a typical study cohort for target protein expression ranges from tens to hundreds; such a small number of datasets is insufficient for high performance model development, and the shortage of public datasets provides limited support in transfer learning. The data requirement sets a high entry barrier for adopting AI-DL technology in clinical research with special stains such as fluorescent stain [19,20]. One conceivable approach for filling this gap is to use color normalization algorithms to compensate for model variation in different staining methodologies, but previous studies have mostly focused on solving the variation in the same colored detection methods [21–23]. Cross-staining recognition to overcome differences between H&E-stained bright field observations and fluorescent nucleic acid-stained dark field observations is yet to be developed.

In this study, we applied color deconvolution (CD) algorithms to normalize the color channels between different staining methods and further integrated them with adaptive color segmentation (ACS) methods to extract the common features of nuclei in the image, thus overcoming the labeling and imaging variations between the color bright field detection and fluorescent dark field detection technologies. We have developed an innovative method for using an H&E-stained segmentation AI model for detailed analysis of fluorescent stained images. This cross-inference expands the application of the current pathology AI models and lowers the barrier for clinical researchers to adopt AI analysis in studies with fluorescent staining image data.

2. Materials and methods

2.1. Sample cohort

In total, 30 breast cancer pathology slides were obtained from the Chi Mei Medical Center (ethical approval identifier: 10,902–002) and stained with H&E.

For fluorescent images, 30 breast cancer samples were acquired from surgical resections at Hsinchu NTUH (ethical approval identifier: 109-053-F) for the testing dataset.

2.2. Image acquisition and ground truth annotation

H&E-stained tissue slides were scanned with a MoticEasyScan scanner using a 20× objective lens (Motic Optical, Hong Kong, China). In fluorescently stained tissue slides, SYTO-16 and DiD fluorescence dyes were used to stain nuclei and cell membranes, respectively, and a Zeiss laser scanning confocal microscope (Carl Zeiss AG, Jena, Germany) with a 20× objective lens was used to obtain the images. The images exported from the equipment were annotated by trained biologists and validated by pathologists using

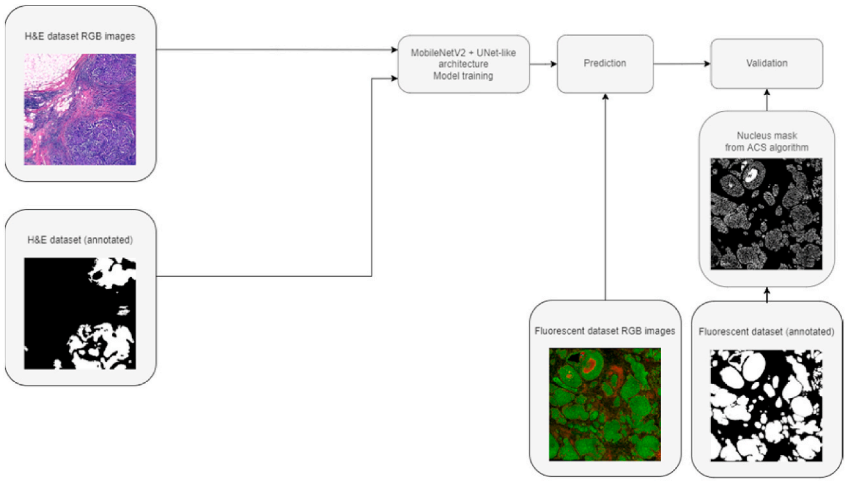

(a)

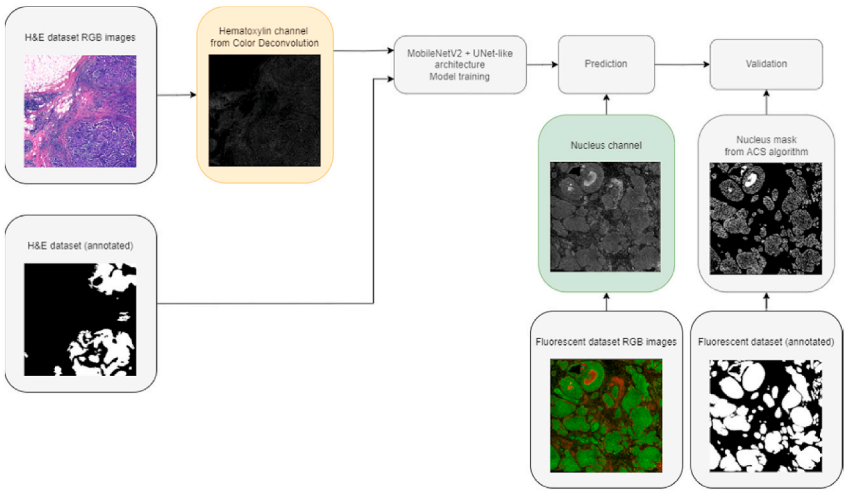

(b)

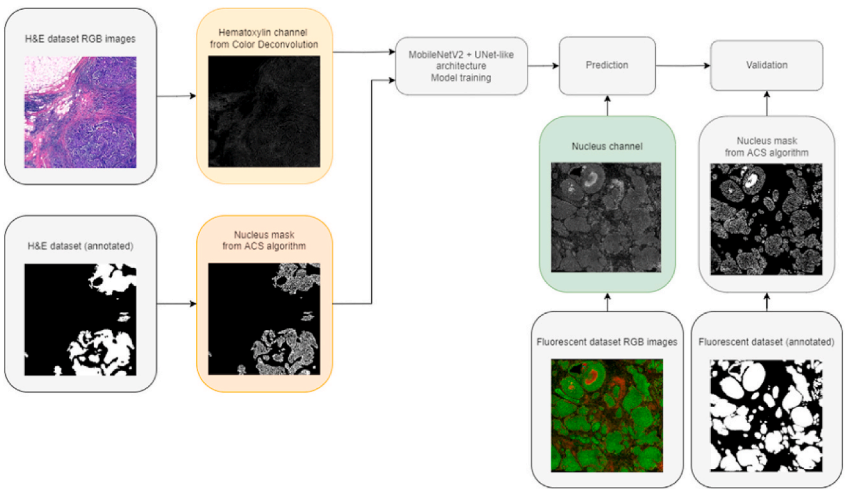

(c)

Fig. 1. Three image training and recognition processes across different staining methodologies and illustrated image examples. (a) Direct use of RGB channels for training and recognition, (b) combination of color deconvolution (CD) algorithms to unify intensity images for training and recognition, (c) combination of CD and adaptive color segmentation (ACS) algorithms for training and recognition.

the open-source computer software MetaLite-RUO (JelloX Biotech Inc., Hsinchu, Taiwan) to identify tumors (including IDC, ILC, and DCIS) and normal regions. In total, 2000 H&E-stained images of 1000 pixels × 1000 pixels in size from 20 cases were randomly selected as the training dataset. In contrast, the H&E testing dataset involved 1000 H&E-stained images from 10 cases, and the fluorescent testing dataset involved 770 fluorescent-stained images with 1000 pixels × 1000 pixels in size from 30 cases.

2.3. Model development with different processing workflows

In this study, three data preprocessing workflows were designed to perform tumor region recognition tasks using different staining methodologies. The procedures for the three different workflows are shown in Fig. 1 (a)–(c). The first approach, shown in Fig. 1(a), applies the original RGB-channeled-image dataset directly for image training and recognition. In this model, complete color information is used for model training. Within the training procedures, a patched image was downsampled four times to satisfy the MobileNetV2 requirements. For example, a patched image with a size of 1000 × 1000 pixels was reduced to 224 × 224 pixels. After the MobileNetV2 encoder module, a U-Net-like decoder was concatenated to avoid gradient vanishing/exploding, and upsampling procedures were performed to go back to 1000 × 1000 pixels for feature classification. Global and local features can be enhanced through down- and up-sampling procedures to facilitate the accurate determination of cancerous regions. Owing to the consistency of the testing accuracy evaluation among different workflows, all testing images were processed with nucleus-mask extraction for later comparison. Finally, the metrics were evaluated by overlapping the regions of the ground truth annotations and model-predicted nucleus masks. The second workflow, shown in Fig. 1 (b), focuses on unifying the intensity features from different staining methodologies. The CD algorithms were applied to separate the nucleus (hematoxylin) channel from the H&E images into grayscale intensity images, and the prediction performance was evaluated by overlapping regions of ground truth annotations and model-predicted nucleus masks. The third workflow depicted in Fig. 1(c) first applies CD transformation to obtain the corresponding intensity channels, followed by integrating an ACS algorithm in tumor annotation masks for nuclei extraction, which further transforms various labeling methods across datasets into single-unified labeling. Illustrated image examples, including the original H&E and IF images, corresponding intensity images, and color-segmented images are shown in Fig. 1.

2.4. Color deconvolution method for color normalization

To overcome substantial difference in color distribution among staining technologies, we generalize the input image by extracting nucleus channel intensity features. For fluorescently stained images, we simply extract the SYTO-16 channel image. For H&E stained images, a channel separation method for bright-field image called Color Deconvolution was used [24]. According to the Beer-Lambert law, with the curated optical density matrix that calculated based on the amount of hematoxylin or eosin stain concentration, we can separate H&E stained RGB image into 2 stain channel signals. After capturing the individual staining signals, the hematoxylin staining

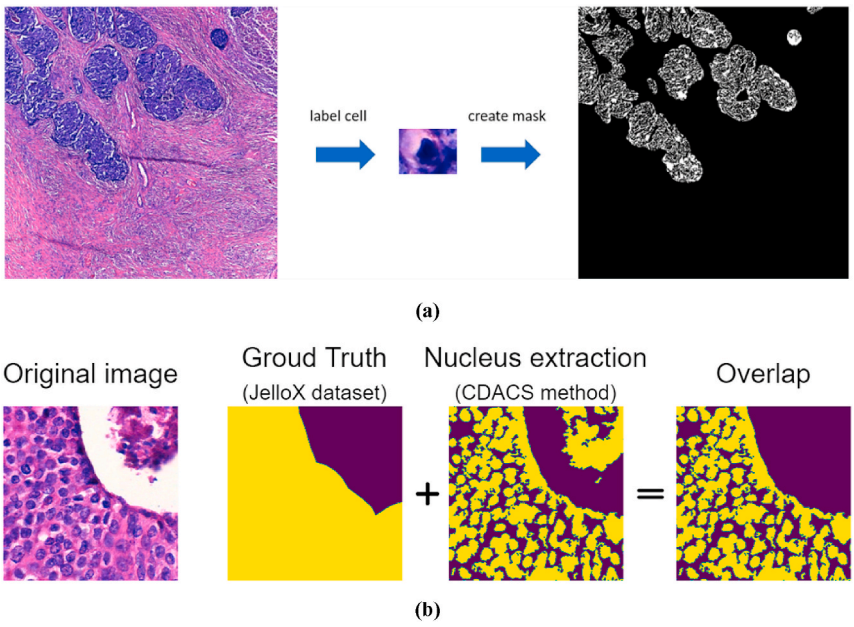

Fig. 2. An example image of accurately annotated cancer nuclei. (a) Use of the ACS algorithm to select interactively and define automatically the image area with the same hue/intensity characteristics; (b) the pathologist manually circled a large area of cancer cells (second from the left) from the original pathological image (first from the left), used the ACS algorithm to extract semi-automatically the identical objects defined as nuclei (third from the left), and finally intersected the lumped area of cancer cells and identified objects to obtain the completely annotated cancer nucleus image.

channel mainly labels nucleus as staining target which paired with SYTO-16 channel from fluorescence images.

2.5. Adaptive color segmentation method for nuclei extraction

To extract nuclei channel information for cross-staining recognition, a semi-automatic analysis technology was developed in this study, based on an ACS algorithm. The analytical process is shown in Fig. 2 (a)-(b). First, a single nucleus or multiple nuclei identified by a pathologist were set as the true nuclei. Then, using the HSV color model transformation, both the hue and intensity channels of selected pixels were statistically analyzed according to distributed histograms and automatically identified with foreground (cancer nucleus) and background (*e.g.,* cytoplasm, cell membrane, empty area) regions using otsu-thresholding. Color segmentation processes were applied to the original image based on the detected hue and intensity distributions of the foreground image. Pixels with similar hue and intensity values were divided into two separate mask areas. After removing salt-and-pepper dotted noise and filling holes to center-less nucleus mask, nuclei mask objects in the region of interest (ROI) were obtained. The ACS method can be interactively selected and defined by the missed cancer nuclei present in the previous steps. Finally, all cancer nucleus objects identified by ACS were intersected with the manually annotated lumped areas by a pathologist to generate clean, detailed cancer nucleus-annotated images.

2.6. Deep neural network model architecture

The prediction model of this study was a convolutional encoder–decoder architecture that used the traditional image segmentation technology and a coarse-to-fine analysis technique for input images. The overall and local features of the images were captured and analyzed. Specifically, the learning model used MobileNetV2 as the encoder [25], which was effective for model training owing to its lightweight features. The U-Net decoder [26] architecture with four upsampling steps of the image segmentation model was applied to the decoding module in the architecture. The residual results of the multi-scale feature layers from the encoder side were combined

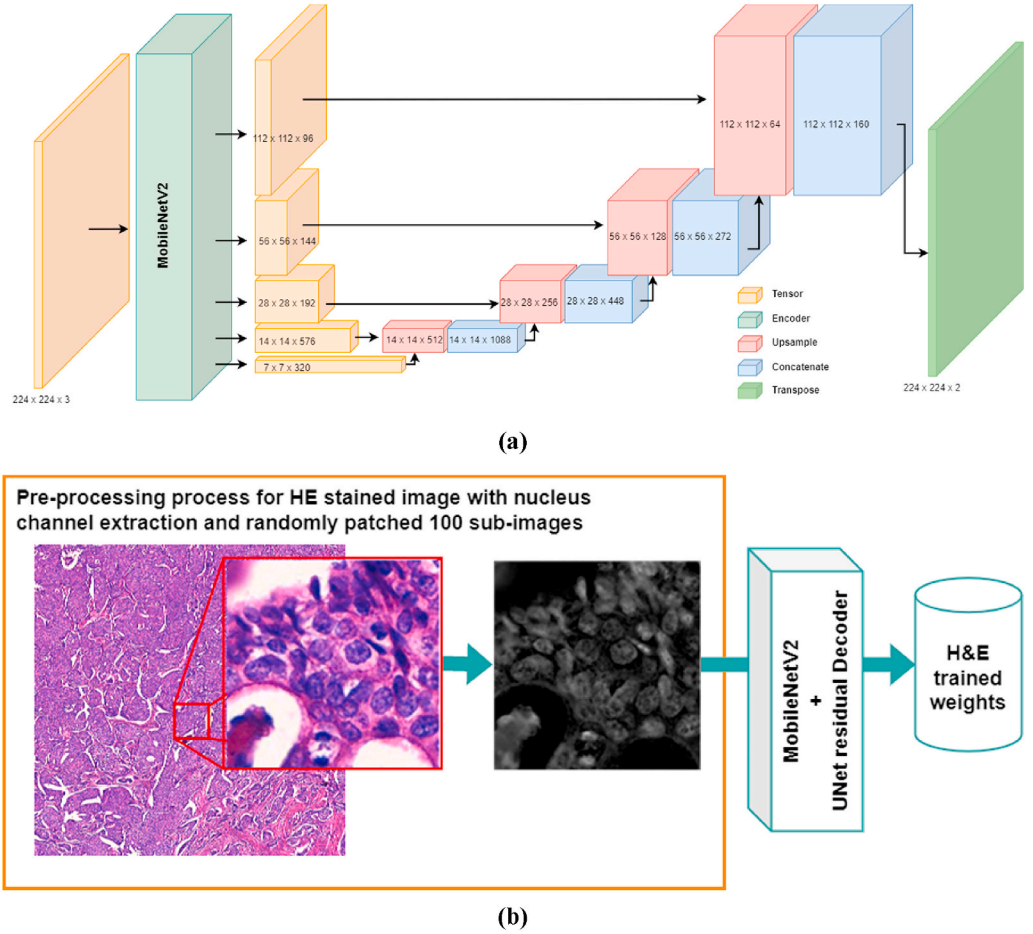

Fig. 3. Combination of model architecture diagrams of MobileNetV2 and U-Net-like architecture with image data flow of the training processes. (a) Detailed-component-level snapshot view for the architecture, (b) visual presentation of training processes with data-preprocessing steps.

with the corresponding upsampled feature layers from the decoder side for stacking. The above design can be used as a tool to solve the problem of gradient vanishing/exploding, an issue often derived from the complexity of current DL models, and to retain the characteristics of the input image at the same time. The complete model architecture is illustrated in Fig. 3 (a).

2.7. Training argument parameter and condition

Details of the training process are shown in Fig. 3 (b). The model with the same architecture was used to train all three workflows accordingly and to deal with the problems of artifacts or obvious outliers at the edges of the patched images. In addition, random patching was adopted, in which the sub-images were trained in batches with 1000 pixels × 1000 pixels as the patch size, the number of random patches was 100 for each complete image, and the best performing weight was selected.

2.8. Model performance evaluation by nucleus instance

In this study, we used nucleus instance accuracy to evaluate the performance of tumor recognition. By executing the computer vision-based nuclei positioning and counting algorithms presented in previous studies [27–29], the tumor nucleus instances within the tumor area delineated by pathologists for all testing images could be obtained. Then, the nucleus instances of the ground truth were compared with those of the tumor area predicted by AI models using intersection over union (IoU), and the corresponding confusion matrices with sensitivities and specificities of the proposed AI models were calculated.

2.9. Additional comparing experiment among nuclei extraction algorithms

We conducted a comparing experiment by using several modern algorithms for nucleus extraction. The dataset used for the validation was obtained from a publicly available nucleus-annotated fluorescence dataset [30]. The comparison was made between our methodology and open-source deep learning algorithms including StarDist, Cellpose, and CellSeg [31–33]. After the segmented nucleus mask was retrieved, we calculated the pixel-wise confusion matrices accordingly with ground truth masks and segmented masks resulting in obtaining F1 scores, sensitivities, and specificities.

3. Results

An additional experiment was conducted to compare the effectiveness of proposed nuclei extraction algorithm. Table 1 showed that our proposed method (ACS) outperformed the other deep learning-based pre-trained methods for nuclear segmentation using fluorescence images. Especially for F1 score, our proposed method could achieve more than 90% while the other algorithms only reached a range between 83% and 89%. Our sensitivity was above 90% and the others were between 74% and 83%, while specificity remained quite similarly high as above 96%.

The training data used with the three data preprocessing workflows are shown in Fig. 4 (a)-(c). The first workflow used RGB-channeled sub-images directly for training. In contrast to the first workflow, the second approach applied CD algorithms to effectively capture the channel signals of individual stains. The nuclei image corresponding to the IF nuclei channel was deconvoluted from the H&E staining images for training. The third workflow further integrated ACS algorithms to reduce the noise of nuclei extraction by using the HSV color space filter, giving a much more accurate nuclei mask, similar to the IF nuclei channel for training processes, which showed possibilities for inferences across different staining methods.

The performance of the breast tumor recognition models trained using the three different data preprocessing workflows was evaluated using two datasets. The first validation applied the H&E staining testing dataset along with the training data using the same visible light dye staining method. Cross-staining recognition was verified by a fluorescent nucleic acid-stained testing dataset that contained a dark field background and fluorescent emission signals. The fluorescent images could be observed with significant differences compared with H&E staining with a white background and visible light signals.

In other words, we tested three different data preprocessing methods on training data preparation, including the original RGB color image, tumor nuclei-only image extracted by CD algorithms, and tumor nuclei-only image extracted by CDACS algorithms, both of which were evaluated to compare differences.

In the H&E-stained testing dataset, the model trained by the original RGB color image showed the best accuracy of 97.6% among the three workflows (Table 2). When compared to other methods, this workflow is the trained a model using a nuclei channel, and an RGB color image containing cytoplasmic information played an important role in the clinical diagnosis of atypical cells, normal cell ducts, and well-differentiated tumor cells. In addition, the RGB color domain training set provided the model with more information

Table 1
Comparison of nuclear segmentation algorithm performances using public fluorescence dataset.

	F1 Score	Sensitivity	Specificity
StarDist	86.7%	81.4%	97.8%
Cellpose	88.3%	82.1%	98.6%
CellSeg	83.0%	74.4%	98.3%
ACS	92.7%	94.6%	96.7%

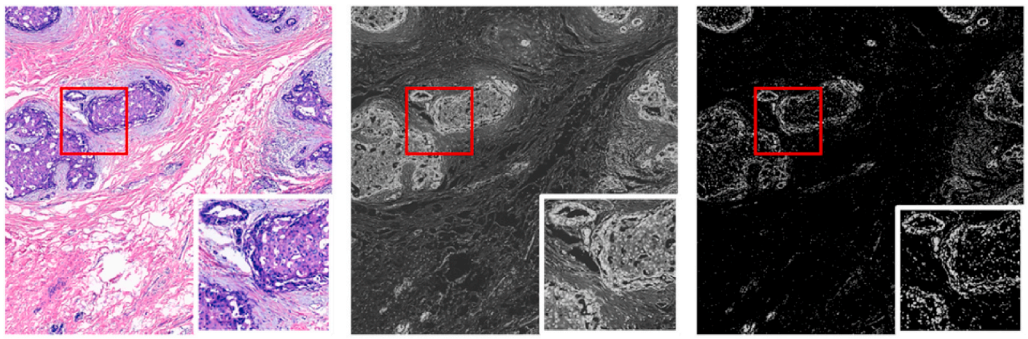

Fig. 4. Training data processed with different data pre-processing workflows. (a) An RGB channeled sub-image; (b) a CD preprocessing sub-image; (c) a CDACS preprocessing sub-image.

for appropriate weight tuning. The inferencing difference is shown visually in Fig. 5 (a); the model trained by the RGB color image performed well on inferencing in atypical cells and the peripheral stroma cells mixed with tumor cells, matching with the pathologist's experiences that require both H&E staining to separate tumor/non-tumor cells accurately in clinical practice. The model trained by the nuclei channel through CD processing performed worse than the RGB color model, resulting in only 83.9% accuracy, revealing that the elimination of cytoplasmic information did influence performance. However, the final CDACS model recovered the performance with an accuracy of nearly 90%. A visualized example showed the capability of general breast tumor nucleus recognition, and the accuracy level was comparable with the typical model performance in previous studies. One possible reason for the difference between the CDACS and CD models might be that CD did not perfectly separate the nuclei channel from the whole image during training dataset preparation, and the incompletely removed cytoplasmic information enhanced the noise in model training.

The testing performance in the fluorescent-stained testing dataset differed from that of the H&E-stained testing dataset. The CDACS model achieved 80.5% testing accuracy, which was significantly higher than that of the other two models, which achieved only 50.4% and 72.5% accuracy using the fluorescent-stained testing dataset (Table 2). The visualized example shown in Fig. 5 (b) demonstrates the differences between the three models. The CDACS model inferred similar breast tumor regions as the manually annotated ground truth; however, the inferencing results of the other two models, especially the model trained by the RGB color image, were far away from the ground truth. Compared to the model performance in H&E-stained testing, the advantage of the RGB color image model in H&E-stained testing turned into a disadvantage in fluorescent-stained testing. Considering that the fluorescently stained image only included the nuclei channel, the cytoplasmic and color domain information in the RGB color image did not contribute to weight derivation but increased noise during model training, leading to a significant drop in accuracy. The CD method separated the nuclei channels during training dataset preparation, but the poor separation performance with residual cytoplasmic information caused worse results than expected. Our proposed novel CDACS model extracts hematoxylin-stained nuclei information equal to the nuclei channel in fluorescent-stained images during the training dataset preparation. Hence, the accuracy dropped by only 9.1% in fluorescent-stained testing as compared to that in H&E-stained testing, indicating that the trained model was applicable to different staining methods and recognized the rest of the tumor region in both H&E− and fluorescent-stained images. However, the nuclei extraction of the CDACS model still resulted in an inevitable drop in accuracy because the model is established relying only on nuclei channel information, making it difficult to distinguish between tumor and normal cells in atypical cells, normal cell ducts, and well-differentiated tumor cells.

4. Discussion and conclusions

This study demonstrates a novel cross-staining recognition algorithm for AI model development using pathology images with various staining methods. By using an integrated workflow of CD and an ACS filter, our CDACS model normalizes the color variation and extracts common features in different staining methods to equalize the training and testing information in cross-staining pathology images. In the performance test using the H&E-stained images trained model for inferring fluorescent images, the typical model

Table 2
Model performance comparison on different stained testing datasets.

	Testing datasets	Accuracy	Sensitivity	Specificity
RGB color model	H&E	97.6%	98.2%	91.5%
	Fluorescent	50.4%	0.0%	100.0%
CD model	H&E	83.9%	48.9%	98.7%
	Fluorescent	72.5%	63.1%	81.7%
CDACS model	H&E	89.6%	84.0%	92.0%
	Fluorescent	80.5%	91.2%	70.0%

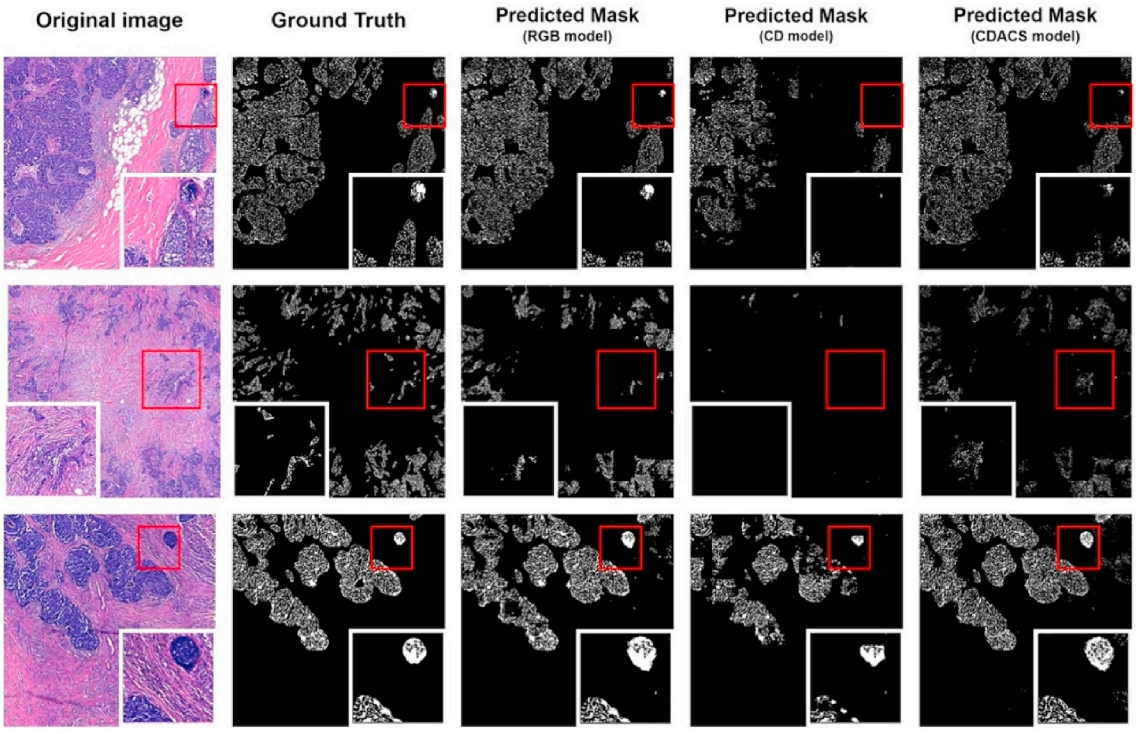

Fig. 5. Inferencing performance of tumor recognition AI models. (a) Performance in H&E image testing dataset; (b) performance in fluorescent image testing dataset.

developed based on RGB color images was inadequate. Even when adopting conventional CD into the workflow for normalizing the difference between staining methods, the model was not able to recognize the fluorescent images well; instead, the H&E inference performance significantly decreased because of poor nuclei separation capability. By taking advantage of the extraction of equalized information in different staining methods, the CDACS model maintained the best testing accuracy on fluorescent images using the H&E image training dataset (80.5%), dropping only 9.1% from the accuracy of inferencing H&E images. Moreover, the testing accuracy of the original H&E images was retained at an acceptable level for general recognition. The results revealed that our algorithm overcame the limitations of the current model development workflow. It was applied to a general model, and thus it could be further applied to a wide range of staining.

Currently, H&E image AI models are well developed for clinical diagnosis, especially for morphological feature recognition of tumors, immune cells, and stoma [17,29,34], owing to the easy data accumulation resulting from daily routine diagnostics. Furthermore, AI can assist pathologists in identifying features related to specific gene mutations and classifying tumors into lung, gastrointestinal, and liver cancers based only on H&E images [35–38]. Computational combination with clinical data, H&E images, and AI reveals some new histological changes of stroma adjacent to the tumor as a tumor microenvironment that are associated with survival prediction, except for well-known prognostic factors in breast cancer and mesothelioma [39,40]. While implementing our proposed novel algorithms, the analysis of fluorescent-stained images in clinical research could also benefit from AI inferencing technologies without the costly generation of a large number of images for building their own models. One of the potential applications of fluorescent-stained images is multiplex staining and analysis in which a particular morphological biomarker, such as panCK or desmin, is labeled to assist in the quantitation of biomarker expression located in a specific region or to study the correlation between biomarkers and morphological features. These morphological biomarkers can eventually be replaced by morphological AI models, creating more opportunities for multiplex research. Three-dimensional (3D) IF staining is another possible application of this CDACS workflow and its related models. Because of tumor heterogeneity, the evaluation of IHC in target protein expression, such as HER2 and PD-L1, is limited by the sampling rate, which causes patient screening error and related low therapy response rates [41,42]. For example, there are still controversies over TIL assessment in breast cancer and PD-L1 quantification, and research for discriminating heterogeneity and subtypes of infiltrating lymphocytes, especially T-cells, according to biomarker expression is increasing [43–45]. Thus, 3D IF staining plays an important role in the discovery of more information on target proteins. As the penetration of antibodies is relatively slow in thick tissue samples, the preparation of 3D IF staining typically takes from several days to several weeks according to the number of biomarkers. The long preparation period makes it reasonable to adopt AI models to recognize morphology in 3D IF images instead of staining multiple morphological biomarkers, thus reducing the turnaround time.

The cross-staining recognition algorithm has the potential to impact various clinical studies. However, restricted information in common features (*e.g.*, nuclei channel only) limits the accuracy of the model. Unrestricted proliferation is a major characteristic of these neoplasms. These cells usually show abnormal morphology, as well as disorganized and expansible growth patterns. However, not all tumors with the same terminology show similar features. Tumors of the same classification may reveal markedly different pathological pictures based on cell morphology and are generally divided into three histological grades: good, moderate, and poor differentiation. Well-differentiated tumors retain most features similar to those of normal cells and tissues, including a relatively typical nuclear contour and organized cell arrangement, which sometimes cannot be distinguished from non-neoplastic tissue in H&E sections, and require other clues, including peripheral tissue reaction or IHC, to assist diagnosis. Poorly differentiated tumors may lose all features of the original cells, and the tumor etiology needs to be confirmed. This study focuses on the cross recognition of tumor nuclei in H&E and fluorescent images and reveals a good correspondence. Nevertheless, nuclei-only recognition has limitations for the identification of well-differentiated tumor cells and normal cells. In poorly differentiated tumors or tumors with marked stromal reactions, such as severe inflammation or fibrosis, pleomorphic and complex nuclear distribution may impede and mislead AI recognition. IHC hematoxylin has been used as a nuclear counterstain, chiefly showing clear nuclear morphology and faint cytoplasmic staining. This cross-staining recognition model may be applied to perinuclear cytoplasmic recognition in the future, which could improve the identification of tumor cells and reveal some interfacial reactions between tumor cells and the peripheral tumor microenvironment.

In summary, this proof-of-principle study provides a clear demonstration of a novel method for cross-staining recognition between H&E-stained bright-field images and fluorescent-stained dark-field images. This is a solution to bridge the image data for parallel analysis using different staining protocols. With appropriate design, this concept has the potential to expand various applications for existing H&E AI models and create more opportunities for fluorescence-based clinical research.

Institutional Review Board Statement: The study was conducted in accordance with the Declaration of Helsinki, and approved by the Institutional Review Board of Chi Mei Medical Center (ethical approval identifier: 10,902–002) and Hsinchu NTUH (ethical approval identifier: 109-053-F).

Informed Consent Statement: Patient consent was waived due to the researches are collecting achieved retrospective samples and involve minimal risk to participants.

Declarations

Author contribution statement

Tun-Wen Pai: Conceived and designed the experiments; Contributed reagents, materials, analysis tools or data; Pei-Wen Huang: Analyzed and interpreted the data; Contributed reagents, materials, analysis tools or data; Wrote the paper.

Hsu Ouyang: Performed the experiments; Wrote the paper.

Bang-Yi Hsu; Yu-Ruei Chang: Performed the experiments.
Yu-Chieh Lin: Conceived and designed the experiments; Wrote the paper.
Yung-An Chen: Conceived and designed the experiments; Performed the experiments; Wrote the paper.
Yu-Han Hsieh: Analyzed and interpreted the data; Wrote the paper.
Chien-Chung Fu; Chien-Feng Li; Ching-Hung Lin; Yen-Yin Lin; Margaret Dah-Tsyr Chang: Contributed reagents, materials, analysis tools or data.

Funding statement

This research did not receive any specific grant from funding agencies in the public, commercial, or not-for-profit sectors.

Data availability statement

Data associated with this study has been deposited at https://www.github.com/JelloXBiotechInc/CD-ACS.

Declaration of interest's statement

The authors declare no conflict of interest.

References

[1] S.K. Suvarna, C. Layton, J.D. Bancroft, Bancroft's Theory and Practice of Histological Techniques. Elsevier, 2019.
[2] A.H. Fischer, K.A. Jacobson, J. Rose, R. Zeller, Hematoxylin and eosin staining of tissue and cell sections, Cold Spring Harb. Protoc. 2008 (5) (2008), https://doi.org/10.1101/pdb.prot4986.
[3] J.A. Ramos-Vara, Technical aspects of immunohistochemistry, Veterinary Pathology 42 (4) (2005) 405–426, https://doi.org/10.1354/vp.42-4-405.
[4] K. Kaliyappan, M. Palanisamy, J. Duraiyan, R. Govindarajan, Applications of immunohistochemistry, J. Pharm. BioAllied Sci. 4 (6) (2012) 307, https://doi.org/10.4103/0975-7406.100281.
[5] L.L. De Matos, D.C. Trufelli, M.G. De Matos, M.A. Da Silva Pinhal, Immunohistochemistry as an important tool in biomarkers detection and clinical practice, Biomark. Insights 5 (2010), https://doi.org/10.4137/bmi.s2185.
[6] G.U.Y. Sainte-Marie, A paraffin embedding technique for studies employing immunofluorescence, J. Histochem. Cytochem. 10 (3) (1962) 250–256, https://doi.org/10.1177/10.3.250.
[7] W.C. Tan, S.N. Nerurkar, H.Y. Cai, H.H. Ng, D. Wu, Y.T. Wee, J.C. Lim, J. Yeong, T.K. Lim, Overview of multiplex immunohistochemistry/immunofluorescence techniques in the era of cancer immunotherapy, Cancer Commun. 40 (4) (2020) 135–153, https://doi.org/10.1002/cac2.12023.
[8] B. Lloyd-Lewis, F.M. Davis, O.B. Harris, J.R. Hitchcock, F.C. Lourenco, M. Pasche, C.J. Watson, Imaging the mammary gland and mammary tumours in 3D: optical tissue clearing and immunofluorescence methods, Breast Cancer Res. 18 (1) (2016), https://doi.org/10.1186/s13058-016-0754-9.
[9] L. Pantanowitz, A. Sharma, A.B. Carter, T. Kurc, A. Sussman, J. Saltz, Twenty Years of digital pathology: an overview of the road travelled, what is on the horizon, and the emergence of vendor-neutral archives, J. Pathol. Inf. 9 (1) (2018) 40, https://doi.org/10.4103/jpi.jpi_69_18.
[10] L. Pantanowitz, N. Farahani, A. Parwani, Whole slide imaging in pathology: advantages, limitations, and emerging perspectives, Pathol. Lab. Med. Int. 23 (2015), https://doi.org/10.2147/plmi.s59826.
[11] L. Hou, D. Samaras, T.M. Kurc, Y. Gao, J.E. Davis, J.H. Saltz, Patch-based convolutional neural network for whole slide tissue image classification, in: IEEE Conference on Computer Vision and Pattern Recognition (CVPR), 2016, https://doi.org/10.1109/cvpr.2016.266.
[12] E. Abels, L. Pantanowitz, F. Aeffner, M.D. Zarella, J. Laak, M.M. Bui, V.N.P. Vemuri, A.V. Parwani, J. Gibbs, E. Agosto-Arroyo, A.H. Beck, C. Kozlowski, Computational pathology definitions, best practices, and recommendations for regulatory guidance: a White Paper from the Digital Pathology Association, J. Pathol. 249 (3) (2019) 286–294, https://doi.org/10.1002/path.5331.
[13] T.J. Fuchs, J.M. Buhmann, Computational pathology: challenges and promises for tissue analysis, Comput. Med. Imag. Graph. 35 (7–8) (2011) 515–530, https://doi.org/10.1016/j.compmedimag.2011.02.006.
[14] L. Barisoni, K.J. Lafata, S.M. Hewitt, A. Madabhushi, U.G. Balis, Digital Pathology and computational image analysis in nephropathology, Nat. Rev. Nephrol. 16 (11) (2020) 669–685, https://doi.org/10.1038/s41581-020-0321-6.
[15] S. Nawaz, Y. Yuan, Computational pathology: exploring the spatial dimension of tumor ecology, Cancer Lett. 380 (1) (2016) 296–303, https://doi.org/10.1016/j.canlet.2015.11.018.
[16] J. Ruan, Z. Zhu, C. Wu, G. Ye, J. Zhou, J. Yue, A fast and effective detection framework for whole-slide histopathology image analysis, PLoS One 16 (5) (2021), https://doi.org/10.1371/journal.pone.0251521.
[17] G. Campanella, M.G. Hanna, L. Geneslaw, A. Miraflor, V. Werneck Krauss Silva, K.J. Busam, E. Brogi, V.E. Reuter, D.S. Klimstra, T.J. Fuchs, Clinical-grade computational pathology using weakly supervised deep learning on whole slide images, Nat. Med. 25 (8) (2019) 1301–1309, https://doi.org/10.1038/s41591-019-0508-1.
[18] The cancer genome atlas program. National Cancer Institute. (n.d.). Available online: https://www.cancer.gov/tcga (accessed on 05/07/2022).
[19] T.K. Leong, W.S. Lo, W.E. Lee, B. Tan, X.Z. Lee, L.W. Lee, J.-Y.J. Lee, N. Suresh, L.-H. Loo, E. Szu, J. Yeong, Leveraging advances in immunopathology and artificial intelligence to analyze in vitro tumor models in composition and space, Adv. Drug Deliv. Rev. 177 (2021), 113959, https://doi.org/10.1016/j.addr.2021.113959.
[20] K. Yamashiro, J. Liu, N. Matsumoto, Y. Ikegaya, Deep learning-based classification of GAD67-positive neurons without the immunosignal, Front. Neuroanat. 15 (2021), https://doi.org/10.3389/fnana.2021.643067.
[21] M.D. Zarella, C. Yeoh, D.E. Breen, F.U. Garcia, An alternative reference space for H&E Color Normalization, PLoS One 12 (3) (2017), https://doi.org/10.1371/journal.pone.0174489.
[22] S. Vijh, M. Saraswat, S. Kumar, A new complete color normalization method for H&E stained histopatholgical images, Appl. Intell. 51 (11) (2021) 7735–7748, https://doi.org/10.1007/s10489-021-02231-7.
[23] J. Boschman, H. Farahani, A. Darbandsari, P. Ahmadvand, A. Van Spankeren, D. Farnell, A.B. Levine, J.R. Naso, A. Churg, S.J.M. Jones, S. Yip, M. Köbel, D. G. Huntsman, C.B. Gilks, A. Bashashati, The utility of color normalization for ai -based diagnosis of hematoxylin and eosin-stained pathology images, J. Pathol. 256 (1) (2021) 15–24, https://doi.org/10.1002/path.5797.
[24] A.C. Ruifrok, D.A. Johnston, Quantification of histochemical staining by color deconvolution, Anal. Quant. Cytol. Histol. 23 (4) (2001) 291–299.
[25] M. Sandler, A. Howard, M. Zhu, A. Zhmoginov, L.-C. Chen, MobileNetV2: inverted residuals and linear bottlenecks, 2018 IEEE/CVF Conf. Comput. Vision Patt. Recognit. (2018), https://doi.org/10.1109/cvpr.2018.00474.
[26] O. Ronneberger, P. Fischer, T. Brox, U-net: convolutional networks for biomedical image segmentation, Lect. Notes Comput. Sci. (2015) 234–241, https://doi.org/10.1007/978-3-319-24574-4_28.

[27] T. Mouroutis, S.J. Roberts, A.A. Bharath, Robust cell nuclei segmentation using statistical modelling, Bioimaging 6 (2) (1998) 79–91, https://doi.org/10.1002/1361-6374, 199806.
[28] G. Begelman, E. Gur, E. Rivlin, M. Radzsky, Z. Zalevsky, Cell nuclei segmentation using fuzzy logic engine, Int. Conf. Image Process. (2004), https://doi.org/10.1109/icip.2004.1421728. *ICIP '04*.
[29] X. Yang, H. Li, X. Zhou, Nuclei segmentation using marker-controlled watershed, tracking using mean-shift, and Kalman filter in time-lapse microscopy, IEEE Transact. Circuits Syst. I: Regular Papers 53 (11) (2006) 2405–2414, https://doi.org/10.1109/tcsi.2006.884469.
[30] F. Kromp, E. Bozsaky, F. Rifatbegovic, L. Fischer, M. Ambros, M. Berneder, T. Weiss, An annotated fluorescence image dataset for training nuclear segmentation methods, Sci. Data 7 (2020) 262, https://doi.org/10.1038/s41597-020-00608-w.
[31] U. Schmidt, M. Weigert, C. Broaddus, G. Myers, Cell detection with star-convex polygons, in: A. Frangi, J. Schnabel, C. Davatzikos, C. Alberola-López, G. Fichtinger (Eds.), Medical Image Computing and Computer Assisted Intervention – MICCAI 2018. MICCAI 2018, Lecture Notes in Computer Science, vol. 11071, Springer, Cham, 2018, https://doi.org/10.1007/978-3-030-00934-2_30.
[32] C. Stringer, T. Wang, M. Michaelos, M. Pachitariu, Cellpose: a generalist algorithm for cellular segmentation, Nat. Methods 18 (2021) 100–106, https://doi.org/10.1038/s41592-020-01018-x.
[33] M.Y. Lee, J.S. Bedia, S.S. Bhate, G.L. Barlow, D. Phillips, W.J. Fantl, G.P. Nolan, CellSeg: a robust, pre-trained nucleus segmentation and pixel quantification software for highly multiplexed fluorescence images, BMC Bioinf. 23 (2022) 46, https://doi.org/10.1186/s12859-022-04570-9.
[34] K. Zhao, Z. Li, S. Yao, Y. Wang, X. Wu, Z. Xu, L. Wu, Y. Huang, C. Liang, Z. Liu, Artificial intelligence quantified tumour-stroma ratio is an independent predictor for overall survival in resectable colorectal cancer, EBioMed. 61 (2020), 103054, https://doi.org/10.1016/j.ebiom.2020.103054.
[35] J. Thagaard, E.S. Stovgaard, L.G. Vognsen, S. Hauberg, A. Dahl, T. Ebstrup, J. Doré, R.E. Vincentz, R.K. Jepsen, A. Roslind, I. Kümler, D. Nielsen, E. Balslev, Automated quantification of stil density with H&E-based digital image analysis has prognostic potential in triple-negative breast cancers, Cancers 13 (12) (2021) 3050, https://doi.org/10.3390/cancers13123050.
[36] M. Chen, B. Zhang, W. Topatana, J. Cao, H. Zhu, S. Juengpanich, Q. Mao, H. Yu, X. Cai, Classification and mutation prediction based on histopathology H&E images in liver cancer using Deep Learning, Npj Precis. Oncol. 4 (1) (2020), https://doi.org/10.1038/s41698-020-0120-3.
[37] N. Coudray, A.L. Moreira, T. Sakellaropoulos, D. Fenyö, N. Razavian, A. Tsirigos, Classification and Mutation Prediction from Non-small Cell Lung Cancer Histopathology Images Using Deep Learning, 2017, https://doi.org/10.1101/197574.
[38] J.N. Kather, A.T. Pearson, N. Halama, D. Jäger, J. Krause, S.H. Loosen, A. Marx, P. Boor, F. Tacke, U.P. Neumann, H.I. Grabsch, T. Yoshikawa, H. Brenner, J. Chang-Claude, M. Hoffmeister, C. Trautwein, T. Luedde, Deep learning can predict microsatellite instability directly from histology in gastrointestinal cancer, Nat. Med. 25 (7) (2019) 1054–1056, https://doi.org/10.1038/s41591-019-0462-y.
[39] P. Courtiol, C. Maussion, M. Moarii, E. Pronier, S. Pilcer, M. Sefta, P. Manceron, S. Toldo, M. Zaslavskiy, N. Le Stang, N. Girard, O. Elemento, A.G. Nicholson, J.-Y. Blay, F. Galateau-Sallé, G. Wainrib, T. Clozel, Deep learning-based classification of mesothelioma improves prediction of patient outcome, Nat. Med. 25 (10) (2019) 1519–1525, https://doi.org/10.1038/s41591-019-0583-3.
[40] A.H. Beck, A.R. Sangoi, S. Leung, R.J. Marinelli, T.O. Nielsen, M.J. van de Vijver, R.B. West, M. van de Rijn, D. Koller, Systematic analysis of breast cancer morphology uncovers stromal features associated with survival, Sci. Transl. Med. 3 (108) (2011), https://doi.org/10.1126/scitranslmed.3002564.
[41] S.S.-Y. Lee, V.P. Bindokas, M.W. Lingen, S.J. Kron, Nondestructive, multiplex three-dimensional mapping of immune infiltrates in core needle biopsy, Lab. Invest. 99 (9) (2018) 1400–1413, https://doi.org/10.1038/s41374-018-0156-y.
[42] Y.-Y. Lin, L.-C. Wang, Y.-H. Hsieh, Y.-L. Hung, Y.-A. Chen, Y.-C. Lin, Y.-Y. Lin, T.-Y. Chou, Computer-assisted three-dimensional quantitation of programmed death-ligand 1 in non-small cell lung cancer using tissue clearing technology, J. Transl. Med. 20 (1) (2022), https://doi.org/10.1186/s12967-022-03335-5.
[43] S. Loi, S. Michiels, S. Adams, S. Loibl, J. Budczies, C. Denkert, R. Salgado, The journey of tumor-infiltrating lymphocytes as a biomarker in breast cancer: clinical utility in an ERA of checkpoint inhibition, Ann. Oncol. 32 (10) (2021) 1236–1244, https://doi.org/10.1016/j.annonc.2021.07.007.
[44] S.E. Stanton, M.L. Disis, Clinical significance of tumor-infiltrating lymphocytes in breast cancer, J. ImmunoTherapy Cancer 4 (1) (2016), https://doi.org/10.1186/s40425-016-0165-6.
[45] P. Savas, R. Salgado, C. Denkert, C. Sotiriou, P.K. Darcy, M.J. Smyth, S. Loi, Clinical relevance of host immunity in breast cancer: from Tils to the clinic, Nat. Rev. Clin. Oncol. 13 (4) (2015) 228–241, https://doi.org/10.1038/nrclinonc.2015.215.